#### Atrascing Auronary and Geophysics

Downloaded from http://mnras.oxfordjournals.org/ at University of Southampton on September 25, 2014

## Long-term wind-driven X-ray spectral variability of NGC 1365 with Swift

S. D. Connolly, <sup>1★</sup> I. M. McHardy <sup>1</sup> and T. Dwelly <sup>1,2</sup>

Accepted 2014 March 17. Received 2014 March 27; in original form 2014 January 6

## **ABSTRACT**

We present long-term (months—years) X-ray spectral variability of the Seyfert 1.8 galaxy NGC 1365 as observed by Swift, which provides well-sampled observations over a much longer timescale (six years) and a much larger flux range than is afforded by other observatories. At very low luminosities, the spectrum is very soft, becoming rapidly harder as the luminosity increases and then, above a particular luminosity, softening again. At a given flux level, the scatter in hardness ratio is not very large, meaning that the spectral shape is largely determined by the luminosity. The spectra were therefore summed in luminosity bins and fitted with a variety of models. The best-fitting model consists of two power laws, one unabsorbed and another, more luminous, which is absorbed. In this model, we find a range of intrinsic 0.5–10.0 keV luminosities of approximately 1.1-3.5 erg s<sup>-1</sup>, and a very large range of absorbing columns, of approximately  $10^{22}$ – $10^{24}$  cm<sup>-2</sup>. Interestingly, we find that the absorbing column decreases with increasing luminosity, but that this result is not due to changes in ionization. We suggest that these observations might be interpreted in terms of a wind model in which the launch radius varies as a function of ionizing flux and disc temperature and therefore moves out with increasing accretion rate, i.e. increasing X-ray luminosity. Thus, depending on the inclination angle of the disc relative to the observer, the absorbing column may decrease as the accretion rate goes up. The weaker, unabsorbed, component may be a scattered component from the

**Key words:** galaxies: active – galaxies: individual NGC 1365 – galaxies: nuclei – galaxies: Seyfert – X-rays: galaxies.

## 1 INTRODUCTION

X-ray spectral observations have shown that variability in the column of absorbing material between the X-ray source and the observer is present in a number of Seyfert galaxies (Risaliti, Elvis & Nicastro 2002). The detection of variable absorption on a timescales of hours has indicated that the absorbing material must be close to the nucleus, at a distance similar to that of the broad emission line region (e.g. Lamer et al. 2003; Elvis et al. 2004; Puccetti et al. 2007), with claims that complete occultations by broad line region clouds have been observed on time-scales of days (Risaliti 2007).

NGC 1365 is a nearby Seyfert 1.8 galaxy (Maiolino & Rieke 1995) which displays a large amount of X-ray spectral variability (Risaliti et al. 2009) on time-scales of hours to years (Brenneman et al. 2013). These variations have been interpreted as the spectrum changing from being 'transmission dominated' to 'reflection dominated'. When the spectrum is 'transmission dominated' (e.g. Risaliti, Maiolino & Bassani 2000), the absorbing material is Compton thin and the transmitted component dominates the spectrum;

\*E-mail: sdc1g08@soton.ac.uk

when the spectrum is 'reflection dominated' (e.g. Iyomoyo et al. 1997), the absorbing material is Compton thick, meaning the majority of direct emission is absorbed and reflected emission dominates the spectrum (Matt, Guainazzi & Maiolino 2003; Risaliti et al. 2007).

A number of absorption and emission lines have been seen in the spectrum. A strong Fe fluorescence emission line is present at 6.4 keV, together with a group of Fe absorption lines between 6.7 and 8.3 keV, attributed to Fe xxv and Fe xxv1 K $\alpha$  and K $\beta$  transitions. The measured velocities of these lines has led to speculation that they originate from a highly ionized, high-velocity outflow from NGC 1365 (Risaliti et al. 2005).

Although there have been many previous X-ray spectral studies of NGC 1365, these studies have all concentrated either on detailed analysis of a single epoch spectrum or on analysis of a small number of spectra taken over a relatively short time-scale (hours or days). By contrast, here we study 190 *Swift* spectra taken over a period of six years. Whilst *Swift* does not provide spectral resolution as high as that used in most previous short-time X-ray spectral studies, e.g. with *XMM—Newton* or *Suzaku*, the *Swift* data cover a much longer time period and a far greater flux range. The *Swift* data therefore allow a proper investigation of flux-related spectral variability

<sup>&</sup>lt;sup>1</sup>University of Southampton, Highfield, Southampton, SO17 1BJ, UK

<sup>&</sup>lt;sup>2</sup>Max-Planck-Institut für Extraterrestrische Physik, Giessenbachstrasse 1, D-85748 Garching, DE

and of long-term spectral variations, over a much larger dynamic range than in previous studies.

The spectrum of NGC 1365, as with most active galactic nucleus (AGN), has previously been modelled using a power-law component, with an intrinsic spectral index,  $\Gamma$ . It is not known whether  $\Gamma$  varies or not during changes in X-ray luminosity. Many groups (e.g. Pounds et al. 2004; Fabian et al. 2005; Turner et al. 2007; Miller, Turner & Reeves 2008) assume that there is no change. Observations in the 2–10 keV band generally do show some variation, although the changes with luminosity are not large (e.g. Zdiarski, Lubi & Smith 1999; Sobolewska & Papadakis 2009). Sobolewska & Papadakis (2009), for example, who simply fit a power law to the 2–10 keV spectra, find that the observed  $\Gamma$  varies as  $2.7\dot{m}^{0.08}$  over similar time-scales to that of our data. In reality, however, these measurements of  $\Gamma$  are, of course, depend on other parameters which were not included in the fits, such as the reflection component and any absorption. If the variation in the observed spectral index is interpreted in terms of the sum of a variable, steep spectrum component and a relatively constant reflection component with a hard spectrum, the intrinsic spectral index can remain constant; in this case, when the flux of the variable steep spectrum component is low, the hard spectrum component dominates, causing the observed spectral index to change (e.g. Guainazzi & Antonelli 1999; Uttley et al. 1999; Fabian & Vaughan 2003; Ponti et al. 2006). Furthermore, where observations with a large spectral range have been made, allowing good definition of the primary continuum slope, the observed variation of  $\Gamma$  with luminosity has not been large (e.g. 0.1 in NGC 4151, Lubiński et al. 2010, 0.2 in NGC 4507, Braito et al.

Theoretical Comptonization modelling (e.g. Coppi 1992; Beloborodov 1999) shows that the photon index can depend on the ratio of  $L_{\rm diss}$  to  $L_{\rm s}$  (where  $L_{\rm diss}$  is the power dissipated in the corona during variations and  $L_{\rm s}$  is the input soft photon luminosity) to a low power (-0.1 for AGN). Unless there are very large variations in these parameters, the intrinsic spectral index should therefore not change by more than a few tenths. Thus, although it is possible that a small change in spectral index may occur over the flux range sampled by our observations, the large changes in  $\Gamma$  required by the pivoting power-law models are assumed to be unlikely. In many of our models, including the model we deem most accurate, we therefore assume  $\Gamma$  to be constant, as this is likely to be a reasonable approximation.

The variability of the spectrum of NGC 1365 has previously been modelled using a partial covering model, in which a varying fraction of the X-ray source is obscured by absorbing material (e.g. Risaliti et al. 2009). This model has been found to fit the data for individual, short time-scale events and is therefore also tested here.

## 2 OBSERVATIONS AND DATA REDUCTION

Observations of NGC 1365 using the *Swift* satellite have been carried out as part of a number of different programmes, the combined data from which has been used in this study. The observations were performed using the *Swift* X-Ray Telescope (XRT) in 'photon-counting mode', between 2006 July 21 and 2013 March 17. A total of 293 spectra from individual *Swift* 'visits', or exposures, were used, with a total of more than 220 ks of exposure time. Individual exposure times ranged from <10 to >1900 s. Data were mostly confined to three main time periods, shown in Table 1. More intensive monitoring took place between MJD 562 20–563 30, due to Supernova 2012fr, which went off in NGC 1365 during this period [but which was neither bright enough nor close enough to the nucleus to

**Table 1.** Summary of *Swift* observations used in this work.  $N_{\text{obs}}$ ,  $N_{\text{visits}}$  and  $T_{\text{tot}}$  are the values remaining after unusable data has been excluded.

OBSIDs	MJD range	Nobs	N <sub>visits</sub>	T <sub>tot</sub> (s)	Cnts <sub>tot</sub>
00035458001-02	539 37.0–539 40.8	2	20	14 714	433
00090101001-09	549 64.0-551 17.5	8	56	44 576	8795
00035458003,					
00080317001,	561 34.1-563 68.5	41	114	105 515	16 227
00032614001-71					
Total	539 37.0-563 68.5	51	190	164 805	25 455

affect the data used in this study (e.g. Klotz, Normand & Conseil 2012; Childress et al. 2013)]. Of the 293 spectra, 103 were rejected due to either very low signal-to-noise or artefacts near the source, leaving 190 usable spectra, consisting of  $\sim 165$  ks of exposure time and over 25 000 photon counts. The raw data for all *Swift* XRT observations of NGC 1365 were downloaded from the HEASARC archive<sup>1</sup>.

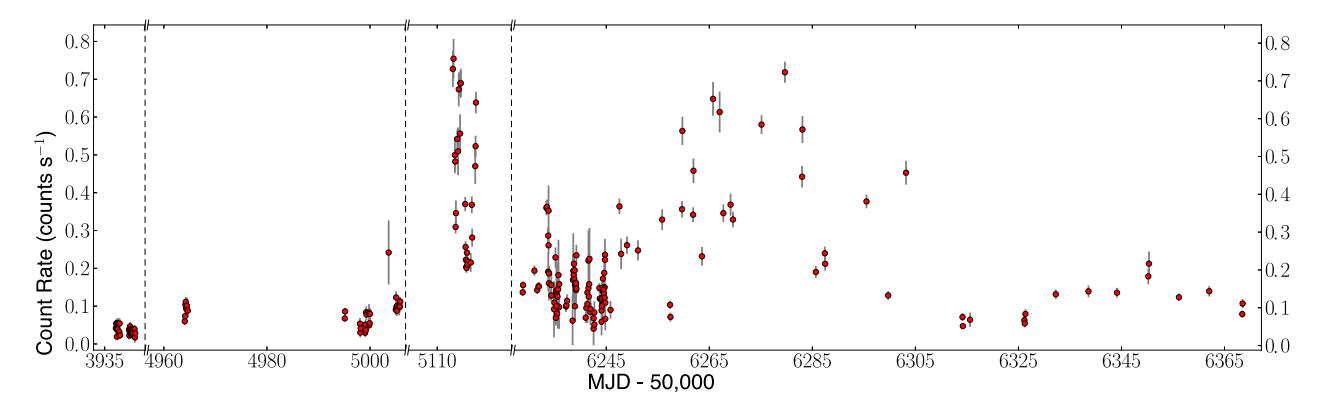
The XRT data were reduced using an automatic pipeline, fully described in Fabian et al. (2012) and previously used in e.g. Cameron et al. (2012). In each case, the reduction used the most recent version of the standard Swift XRTPIPELINE software (versions 0.12.4–0.12.6). The XSELECT tool was used to extract spectra and light curves, using flux-dependent source and background-extraction regions which were chosen such as to reduce the background contamination at faint fluxes, and to mitigate the effects of pile-up at high fluxes. The sensitivity of the XRT is not uniform over the field of view, due to vignetting and the presence of bad pixels and columns on the CCD; the Swift XRTEXPOMAP and XRTMKARF tools were therefore used to generate an exposure map (including vignetting and bad pixels) and an ancillary response file for each visit, in order to correct for these effects. The relevant redistribution matrix file from the Swift calibration data base was also supplied in each case. The local X-ray background was estimated and subtracted from the instrumental count rates, using the area-scaled count rate measured in a background annulus region. The observed XRT count rates were carefully corrected for the fraction of counts lost due to bad pixels and columns, vignetting effects, and the finite extraction aperture (including regions excised in order to mitigate pileup effects).

Fig. 1 shows a 0.5–10.0 keV light curve of all of the *Swift* data over the six-year period of observation. The large flux range is readily apparent on a range of time-scales.

Chandra images show that the nucleus of NGC 1365 is embedded within a region of extended low surface brightness emission, of radius approximately 15 arcsec (see Wang et al. 2009). The region used to determine the Swift background contribution lies outside this small region of extended emission. Thus, a contribution from the constant extended emission within the Swift point spread function (PSF) will remain in our Swift spectra. To determine what that contribution is, we examined Chandra spectra of the extended emission region. The Chandra data used were taken in 2002 December, using the ACIS-S instrument (OBSID 3554). Four spectra were extracted from circular regions, of size similar to the Swift PSF, lying close to the nucleus. The spectra were extracted from the event files in the primary (reduced) data set, using the CIAO 4.6 tool 'SPECEXTRACT'. Extraction regions of radius 2 arcsecs were used in each case.

The background spectra were taken from within the same region from which the *Swift* background spectra were taken, such that the

http://heasarc.gsfc.nasa.gov/cgi-bin/W3Browse/swift.pl



**Figure 1.** The *Swift* X-ray light curve of NGC 1365, with a broken axis where data were not taken. The section on the right shows the period during which more intensive *Swift* monitoring was taking place as a result of SN2012fr.

resultant spectra did not contain the background which had been subtracted from the *Swift* spectra. Circular extraction regions of radius 2 arcsecs were also used.

#### 3 DATA ANALYSIS

## 3.1 Spectral hardness

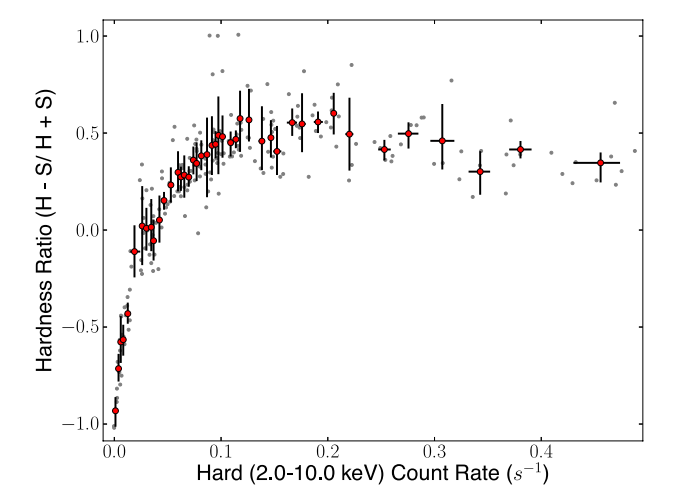
Plots of the hardness ratio against the hard count rate, and the hard count rate against the soft count rate are shown in Fig. 2. Whereas most previous measurements of the photon index,  $\Gamma$ , concentrate on the 2.0–10.0 keV energy band; here, we look at spectral shape across a broader range of 0.5–10.0 keV. As lower energies are more sensitive to absorption, this energy range allows a more complete look at spectral changes due to absorbing material. In each case, hard emission is defined as 2.0–10.0 keV and soft emission as 0.5–2.0 keV. The hardness ratio is defined as

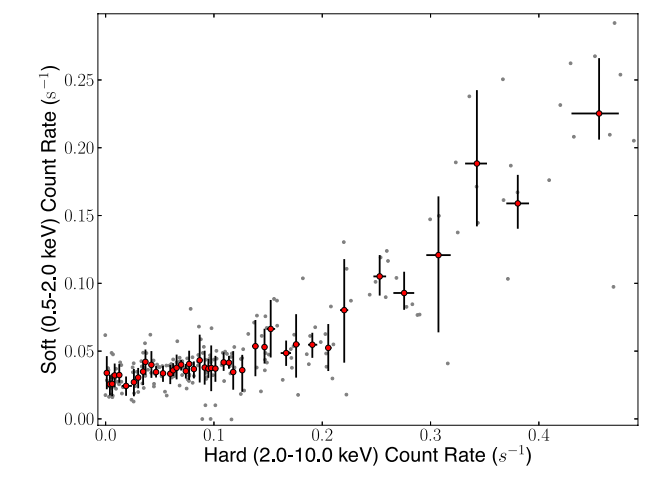
$$Hardness Ratio = \frac{Hard Cnt Rate - Soft Cnt Rate}{Hard Cnt Rate + Soft Cnt Rate}.$$
 (1)

Fig. 2 shows the spectrum to be extremely soft at very low fluxes, but to become hard very rapidly with increasing flux. Beyond this sharp rise, still at a relatively low flux, the hardness decreases again more gradually with increasing flux, as often seen in Seyfert galaxies within the 2.0–10.0 keV band (e.g. Lamer et al. 2003; Sobolewska & Papadakis 2009). The data display a relatively small amount of scatter about this general trend; for this reason, the shape of the spectrum can be assumed to be approximately similar at a given flux level, independent of time. This implies that the system is behaving in approximately the same manner at each flux level, irrespective of what state the system was in at an earlier time, allowing flux binning of spectra to improve the signal-to-noise ratio.

## 3.2 Spectral modelling

The 190 separate time-resolved XRT spectra of NGC 1365 were divided into 11 flux bins and combined using the HEADAS tool 'addspec' (see Fig. 3 for a sample of these summed spectra). The bins were chosen such that each binned spectrum had both a minimum of 2000 total counts and a minimum width of 0.025 counts s<sup>-1</sup> across the total range of hard count rates. This binning method ensured that each summed spectrum would possess a sufficient signal-to-noise ratio for accurate spectral fitting, and that the flux





**Figure 2.** Top: plot of the hard count rate against hardness ratio of NGC 1365. The scatter around the mean at a given count rate is low. Bottom: plot of the hard count rate against soft count rate of NGC 1365. In both plots, the data are binned such that each bin contains a minimum of five data points. Errors in the hard count rate are the standard deviations of the distribution of points in each bin. The unbinned data are shown lightly behind the binned data. The typical fractional errors on the unbinned data are 0.16, 0.22 and 0.38 for the soft counts, hard counts and hardness ratio, respectively.

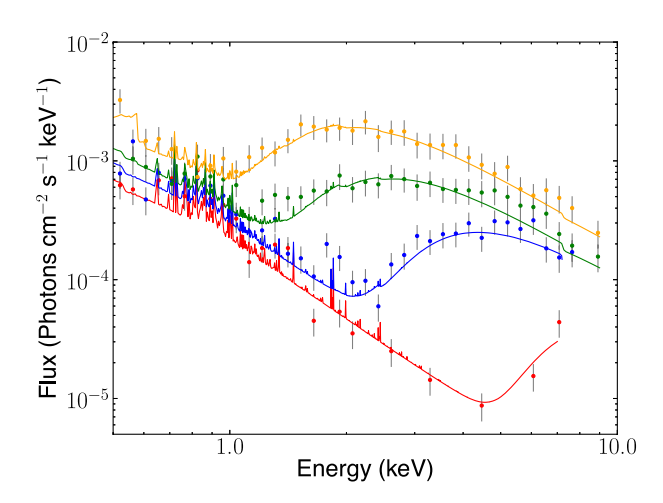


**Figure 3.** A sample of the set of unfolded, summed spectra produced by combining spectra in the same flux range. Alternate spectra are excluded, to prevent the plot being crowded. The spectra are simultaneously fitted with the best-fitting model, consisting of two power laws, one of which is absorbed by a partially ionized absorbing column and one of which is not. Both power laws have a fixed spectral index of 1.92, as found by Risaliti et al. (2013). The ionization state of the absorbing material is tied, but the absorbing column is allowed to vary between individual fits, producing the variation seen between spectra from different flux levels. The flux values are calculated by XSPEC using the model. The data are binned for clarity.

bins were roughly evenly spaced across the hard flux range covered by the spectra. The energy channels of each of these summed spectra were then grouped, using the HEADAS tool 'grppha', such that each group contained a minimum of 15 counts.

A variety of models were fitted to the spectra, using the XSPEC 12.7 analysis package (Arnaud 1996). The models were simultaneously fitted to all 11 summed spectra, in order to discover the cause of variations in the shape of the spectrum with changing flux. In each case, parameters were either fixed at a single value for all spectra, 'tied' such that the parameter was allowed to vary but was the same for all 11 spectra, or left free to vary between the fits to individual spectra.

To account for the diffuse emission surrounding the nucleus of NGC 1365 (see Section 2), the four *Chandra* spectra were fitted. These spectra were composed of a minimum of 1300 counts. The spectral energy channels were grouped in the same way as the *Swift* spectra, such that each group contained a minimum of 15 counts.

As found previously by Wang et al. (2009), the best-fitting model is the apec model for collisionally ionized diffuse gas combined with the *tbabs* model for absorption by gas and dust. These models were used together with the wabs model, to account for the known galactic absorption along the line of sight  $(1.39 \times 10^{20} \text{ cm}^{-2})$ . A simultaneous fit to four regions, allowing  $N_H$  to vary, but with all other parameters tied, gave a reduced  $\chi^2$  of 0.96, with 197 degrees of freedom. The absorbing column varied a little between regions. However, as a single value is required to fit the average contribution to the Swift nuclear spectrum, we fitted all regions with the same  $N_H$ , giving a reduced  $\chi^2$  of 1.46, with 200 degrees of freedom. In this model, the best-fitting parameters were: an absorbing column of  $6.97^{+0.02}_{+0.02} \times 10^{20}$  cm<sup>-2</sup> in addition to galactic absorption, a gas temperature of  $0.77^{+0.03}_{+0.03}$  keV, a metal abundance of  $0.069^{+0.010}_{+0.012}$ and a normalization of the apec model of  $5.51^{+0.63}_{+0.73} \times 10^{-4}$ . The components of this model, with each of the parameters fixed at the best-fitting values, were included in all of the subsequent fits of the Swift data.

When modelling the resultant XRT background-subtracted nucleus, it was discovered that a single, unabsorbed power law of photon index  $\sim$ 1.92 (as found by Risaliti et al. 2013), fitted the lowest flux observations very well, except for a small excess at higher energies ( $>\sim$ 4.0 keV). With increasing total flux, this excess was seen both to increase in flux relative to the lower energy component and to expand to lower energies, such that the single power-law model become increasingly inadequate.

At the highest fluxes, it was found that a single power law would fit the data very well if absorbed by a partially ionized absorbing column. This model was, however, still insufficient to give a good fit at intermediate fluxes, as these spectra had a comparable flux at both the low- and high-energy ends of the spectra.

Motivated by the steep unabsorbed spectrum, with its high-energy excess, found at low fluxes, and the absorbed component found at the higher fluxes, a set of two-component models were fitted to the data. These models consisted of two power laws, one of which was unabsorbed and the other absorbed, with the absorbing column and ionization parameter left as either free or tied parameters (see models 1–4 in Table 2). These models were found to fit the data well in simultaneous fits of the spectra from all flux ranges. The column of the absorbing material, and its ionization parameter, were either tied or left to vary between individual spectra. The matrix of the variations of each model, together with each goodness of fit, is given in Table 2. Typical values of the parameters in each model are given in Table 3.

In these two-component models, the two power laws had the same spectral index,  $\Gamma$ , fixed at the value found by Risaliti et al. (2013) using the very wide spectral range allowed by *NuStar*. It was possible to obtain equally good fits at all fluxes using a single absorbed pivoting power law and better fits using two pivoting power laws of the same spectral index (see models 6–11 in Table 2). However, the best-fitting models of this kind required a very large range of  $\Gamma$  (from  $\sim 0.6$  to  $>\sim 1.8$ ), and, very unusually, an extremely low value of  $\Gamma$  at high fluxes. As described in Section 1, this is considered to be unphysical over the observed luminosity range.

In all models, the absorbed power law was modelled using the *absori* model for an ionized photoelectric absorber. The absorber temperature was tied in all fits. A redshift of  $5.569 \times 10^{-3}$  (Lavaux & Hudson 2011) and an iron abundance of 2.8 times solar abundance, as found by Risaliti et al. (2009), were used in all fits. Galactic absorption of  $1.39 \times 10^{20}$  cm<sup>-2</sup> was also included in each model, using the *wabs* model for electromagnetic absorption (Dickey & Lockman 1990).

The effects of Compton Scattering on the fits were tested by adding the *cabs* model in xspec (see model 12 in Table 2). The inclusion of this model was found to have very little effect on the best-fitting parameters, or the goodness of fit. This result is not unexpected, as the highest measured absorbing column is  $1.0 \times 10^{24} \, \mathrm{cm}^{-2}$ , which is below the column required to be Compton thick  $(1.5 \times 10^{24} \, \mathrm{cm}^{-2}$ , see Malizia et al. 2009).

In model 3 of Table 2, the absorbing column is neutral, i.e. the ionization state is fixed at zero. The best-fit in this model is almost the same as those in which the ionization is free (models 1 and 2). Thus, although the value of the absorbing column has a large effect on our fits, the ionization state is not well constrained.

Finally, a set of partial covering models were fitted to the data, as this type of model has previously been found to be successful in modelling changes over short time-scales (e.g. Risaliti et al. 2009; see models 13–15 in Table 2). The model (*pcfabs* in XSPEC) consists of a neutral absorber which covers a fraction of the X-ray source, resulting in a spectrum composed of an absorbed and an unabsorbed

range of values for the spectral index,  $\Gamma$ , which was fixed or best fitting. The reduced  $\chi^2$  value and number of degrees of freedom (DoF) of the best fit with each model is also Table 2. Summary of the main components of each model fitted to the average spectra, showing the parameters which were fixed, tied or left free in each case, and the value or shown. Each model also contains the fixed components of the best-fitting model to the diffuse gas around the nucleus (tbabs\*apec) and the entire model is multiplied by the wabs model set to the galactic absorbing column

Model	xspec description	Spectral index	Spectral index Absorbing column Ionization	Ionization	Г	$\chi^2_{ m Red}$	DoF
Absorbed and unabsorbed power laws	powerlaw + absori × powerlaw	Fixed	Free	Free	1.92 (fixed)	1.39	1329
Absorbed and unabsorbed power laws	powerlaw $+$ absori $\times$ powerlaw	Fixed	Free	Tied	1.92 (fixed)	1.42	1339
Absorbed and unabsorbed power laws	powerlaw $+$ absori $\times$ powerlaw	Fixed	Free	0	1.92 (fixed)	1.44	1340
Absorbed and unabsorbed power laws	powerlaw $+$ absori $\times$ powerlaw	Fixed	Tied	Free	1.92 (fixed)	2.28	1339
Absorbed and unabsorbed power laws	powerlaw $+$ absori $\times$ powerlaw	Tied	Free	Free	1.47 (tied)	1.21	1328
Absorbed and unabsorbed power laws	powerlaw $+$ absori $\times$ powerlaw	Free	Free	Free	1.22 - 2.09	1.17	1318
Absorbed and unabsorbed power laws	powerlaw $+$ absori $\times$ powerlaw	Free	Free	Tied	1.19 - 2.09	1.20	1328
Absorbed and unabsorbed power laws	powerlaw $+$ absori $\times$ powerlaw	Free	Tied	Free	0.30 - 1.78	1.86	1328
Single, absorbed power law	absori × powerlaw	Free	Free	Free	0.61 - 1.81	1.36	1328
Single, absorbed power law	absori × powerlaw	Free	Free	Tied	0.58 - 1.82	1.63	1328
Single, absorbed power law	absori $\times$ powerlaw	Free	Tied	Free	0 - 1.91	1.42	1318
Compton scattering	$(powerlaw + absori \times powerlaw) \times cabs$	Fixed	Free	Tied	1.92 (fixed)	1.42	1339
Partial covering, fraction tied	$pcfabs \times powerlaw$	Fixed	Tied	n/a	1.92 (fixed)	2.57	1351
Partial covering, fraction tied	$pcfabs \times powerlaw$	Fixed	Free	n/a	1.92 (fixed)	1.45	1351
Partial covering, fraction free	pcfabs × powerlaw	Fixed	Free	n/a	1.92 (fixed)	1.45	1341

component. We found that the data could not be well fit by a model in which the absorbing column is constant between spectral fits, with only the covering fraction changing (model 13). If we allow the absorbing column to vary, we obtain the same quality of fit whether we allow the covering fraction to vary (model 14) or not (model 15), as, when the fraction is allowed to vary, the same value is derived at each flux level. Model 14 is physically very similar to our two component model (model 2).

## 3.3 Two-component spectral variability

In all fits described here, we fix the underlying power-law spectral index at the value given by Risaliti et al. (2013). Allowing  $\Gamma$  to vary does give better fits but, as discussed above, the required range of  $\Gamma$  is extremely large and almost certainly unphysical.

In the two-component models with a fixed  $\Gamma$ , leaving the ionization state to vary, but tying the absorbing column, was found to be insufficient to account for the degree of variation observed in the spectra, at any fixed absorbing column, for both a pivoting power law and the two-component model, as can be seen from the  $\chi^2$  values.

Tying the ionization state whilst leaving the absorbing column free to vary, however, gives good fits to the data. Significantly, the  $\chi^2$  value is very similar to that of the model in which both the ionization state and absorbing column are both left free to vary, as the ionization varies little in the best-fitting model. Whilst the ionization state of the absorbing material undoubtedly changes, the data show both that large changes are not required to give a good fit, and that large changes in the absorbing column are essential to account for the spectral variation observed regardless. Changes in ionization alone cannot account for these spectral changes observed. The two-component model with one absorbed and one unabsorbed power law, in which the absorbing column is left free to vary between spectra whilst the ionization state is kept constant, is therefore the simplest model with which the spectral variability seen in the data can be described.

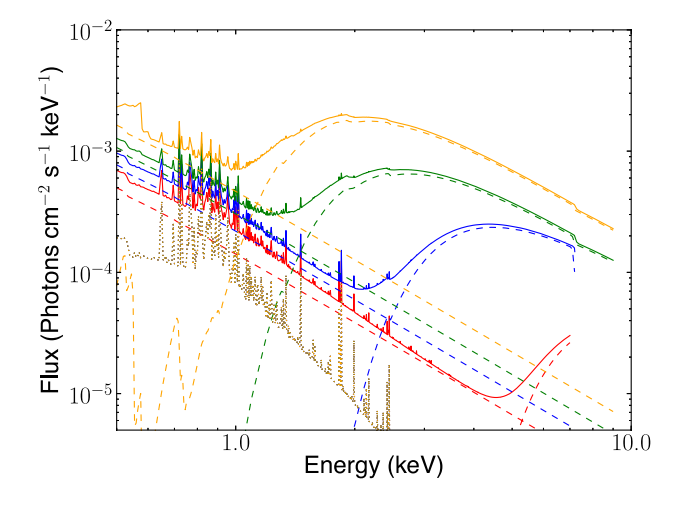
In this model, there was a large range of absorbing columns, from  $1.69\times 10^{22}$  to  $10^{24}~cm^{-2}.$  The temperature of the absorber was  $9.5\times 10^5~K$  and the ionization state of the absorber was 0.11. The normalizations of the two power laws varied by a factor of 3, giving a range of intrinsic luminosities of approximately 1.1 to 3.5 erg s $^{-1}$  for the 0.5--10.0~keV band.

Fig. 3 shows a sample of the flux-binned spectra fitted with this model. Fig. 4 shows how the two power-law components vary as the flux changes. The plot shows that the absorbing column of the absorbed power law decreases as the normalization of the power law (i.e. the flux before absorption) increases. These two parameters are plotted in Fig. 5. There is a strong decrease in the absorbing column as the normalization increases (Spearman ranked correlation coefficient  $\rho=0.98^{+0.02}_{-0.20}$ ), but the data are not of sufficient quality to precisely determine the form of the relationship between these parameters.

In Fig. 6, the normalization of the unabsorbed power law is plotted against that of the absorbed power law. The normalizations can be fitted well with a linear model, showing them to be correlated (r=0.91). These observations confirm that there is a real change in the underlying luminosity of the source and that the observed flux changes are not just due to changes in absorption. The  $15-150~\rm keV$  Burst Alert Telescope (BAT) light curve of NGC 1365, which undergoes far less absorption than the  $0.5-10~\rm keV$  band, confirms this intrinsic variability, showing variation of approximately a factor of 4.

**Table 3.** Typical parameter values for each model described in Table 2, taken from the fit to the spectrum of the central flux bin. 90 per cent errors are given where a parameter was free or tied. Errors for models with an asterisk (\*) are not given, as the reduced  $χ^2$  of the fit was >2, preventing their calculation in xspec. As the absorber temperature in models 5 and 6 reached the upper limit of the *absori* model, the positive errors on these values (indicated with †) are given as zero. These values are, however, unconstrained in the positive direction. The parameters are as follows: Γ – spectral index,  $N_H$  – absorbing column ( $10^{22}$  cm<sup>-2</sup>),  $n_A$  – normalization of the absorbed power law ( $10^{-4}$  keV<sup>-1</sup>cm<sup>-2</sup>s<sup>-1</sup> at 1 keV),  $n_U$  – normalization of the unabsorbed power law ( $10^{-4}$  keV<sup>-1</sup>cm<sup>-2</sup>s<sup>-1</sup> at 1 keV), ξ – ionization state ( $L_{5-300\text{keV}}/N_eR^2$  – see Done et al. 1992), T – absorber temperature ( $10^5$  K), F – covering fraction.

Model	Γ	$N_{\mathrm{H}}$	$n_{\rm A}$	$n_{\mathrm{U}}$	ξ	T	F
1	1.92	$9.48^{+1.50}_{-1.72}$	97.4 <sup>+8.2</sup> <sub>-8.3</sub>	$3.53^{+0.41}_{-0.42}$	$11.44^{+5.57}_{-3.50}$	10.00 <sup>+0.00†</sup> <sub>-3.57</sub>	_
2	1.92	$6.03^{+0.85}_{-0.61}$	$90.2^{+9.1}_{-7.0}$	$3.73^{+0.37}_{-0.35}$	$0.41^{+0.36}_{-0.36}$	$5.90^{+4.10}_{-0.29}$	_
3	1.92	$5.82^{+0.77}_{-0.69}$	$92.1^{+8.7}_{-8.1}$	$3.80^{+0.36}_{-0.36}$	0	_	_
4*	1.92	5.44	84.6	3.63	0.017	10.00	_
5	$1.41^{+0.05}_{-0.06}$	$8.33^{+1.84}_{-2.18}$	$38.2^{+4.4}_{-4.1}$	$0.395^{+0.44}_{-0.46}$	$19.27^{+12.63}_{-16.26}$	$10.00^{+0.00\dagger}_{-2.56}$	_
6	$1.22^{+0.16}_{-0.18}$	$7.97^{+2.08}_{-2.52}$	$25.8^{+10.3}_{-8.1}$	$3.95^{+0.46}_{-0.48}$	$30.99^{+41.85}_{-30.99}$	$10.00^{+0.00\dagger}_{-3.22}$	_
7	$1.19^{+0.16}_{-0.17}$	$5.01^{+0.94}_{-0.86}$	$23.8^{+9.4}_{-7.3}$	$4.20^{+0.40}_{-0.40}$	$0.15^{+0.65}_{-0.15}$	$3.40^{+6.60}_{-2.85}$	_
8	$1.23^{+0.12}_{-0.28}$	$8.84^{+0.55}_{-0.62}$	$27.1_{-9.0}^{+7.6}$	$4.01_{-0.46}^{+0.44}$	$43.21^{+65.38}_{-14.99}$	$7.60^{+7.60}_{-2.03}$	_
9	$0.70^{+0.07}_{-0.05}$	$3.91^{+0.59}_{-0.79}$	$10.9^{+0.1}_{-0.1}$	_	$357.0^{+55.5}_{-46.6}$	$3.04_{-0.38}^{+0.80}$	_
10	$0.79^{+0.04}_{-0.04}$	$3.84^{+0.78}_{-0.75}$	$12.5^{+1.3}_{-1.2}$	_	$288.0^{+23.0}_{-21.8}$	$2.70_{-0.32}^{+0.38}$	_
11	$0.55^{+0.08}_{-0.05}$	$1.29^{+0.08}_{-0.07}$	$7.77^{+0.1}_{-0.1}$	_	$708.0^{+334.0}_{-197.3}$	$0.28^{+0.10}_{-0.05}$	_
12	1.92	$6.12^{+0.78}_{-0.66}$	$91.2^{+8.4}_{-7.6}$	$3.75^{+0.36}_{-0.36}$	$0.39^{+0.38}_{-0.35}$	$0.56^{+9.54}_{-0.29}$	_
13*	1.92	4.51	73.7	-	-	-	0.952
14	1.92	$7.50^{+0.68}_{-0.78}$	$100.1_{-4.3}^{+9.3}$	_	_	_	$0.963^{+0.001}_{-0.006}$
15	1.92	$7.57^{+0.95}_{-0.85}$	$102.7^{+5.7}_{-7.1}$	_	_	_	$0.967^{+0.02}_{-0.001}$



**Figure 4.** The sample of best-fitting models shown in Fig. 3 (solid lines), together with the components of each model – the unabsorbed power law and absorbed power law (dashed lines), and the spectrum of the underlying diffuse emission (dotted line).

As a consistency check, the hard count rate and hardness ratio from each model fitted to the summed data are plotted over the original data as in Fig. 2 (Fig. 7). These plots show that the summed spectra also follow the trends shown by the individual spectra, reinforcing the assumption that the spectrum is similar at a given flux level, independent of time.

A two component spectral model consisting of an unabsorbed scattered component and a more luminous absorbed component has previously been used to describe the single epoch spectrum of NGC 4945 (Done, Madejski & Smith 1996). Broadly similar two-component spectra are also reported elsewhere (e.g. NGC4507, Braito et al. 2012). Variations of hardness ratio versus count rate similar to those shown here, in Fig. 2, have also been seen in the

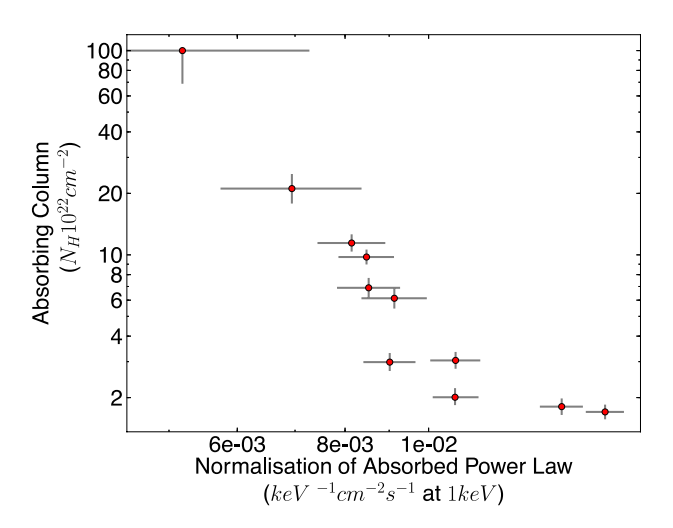


**Figure 5.** Log plot of the normalization parameter of the absorbed power law against the column of the absorbing material in the model described above (model 2 in Table 2). The normalization of the power law is equivalent to the flux of this component before absorption, and therefore the X-ray luminosity of the source.

spectra of X-ray binary systems (fig. 1 in Kuulkers et al. 1998) from *RXTE* data (2–13 keV). Although Kuulkers et al. (1998) do not discuss flux-binned spectra as seen in our Fig. 3, they also favour a similar two component model. These studies show that a two component model broadly similar to that which we describe here can, not infrequently, be used to parametrize the X-ray spectra of both AGN and X-ray binary sources. However, the main contribution of this paper is to show, for the first time, that the complete, and very large, range of spectral variability displayed by at least one AGN can be explained by systematic variation of the absorber, with the absorption varying inversely with luminosity. Below we discuss a possible model to explain this behaviour.

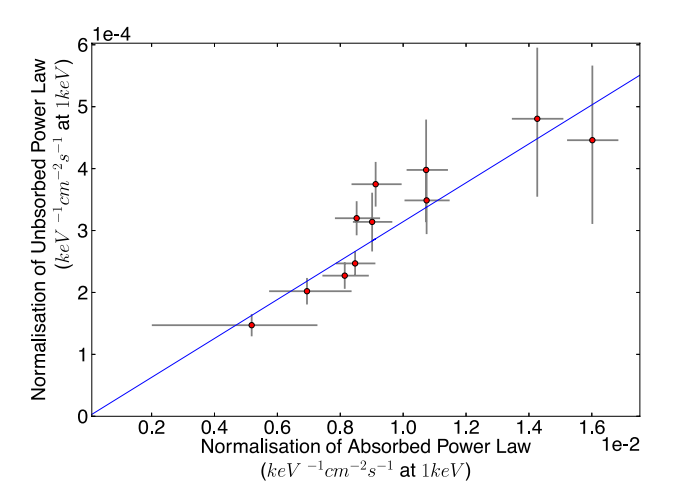


**Figure 6.** Plot of the normalization parameter of the absorbed power law against the normalization parameter of the unabsorbed power law in the model described above (model 2 in Table 2). These normalizations are equivalent to the unabsorbed flux from each component; the correlation between them implies that the two components originate from the same source. The data are fitted with a linear model going through the origin, with a reduced  $\chi^2$  of 1.50 for 10 degrees of freedom.

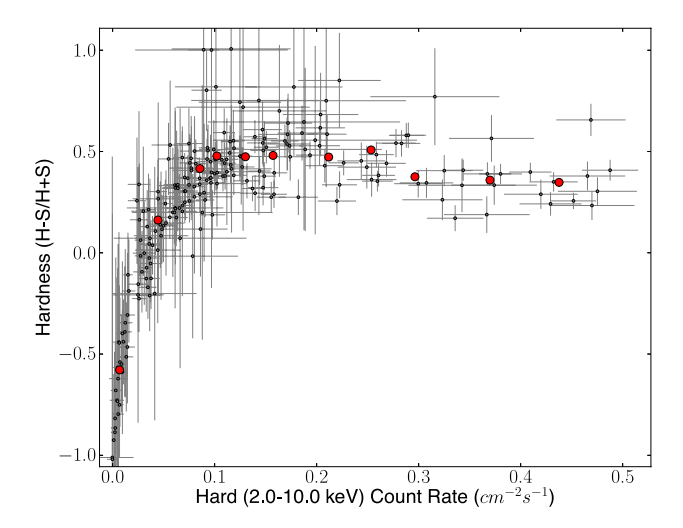


**Figure 7.** Plot of the hardness against the hard count rate of each of the 190 observed spectra (small circles), together with that of the model spectra described above (model 2 in Table 2) when fitted to each of the 11 summed, flux-binned spectra (large circles).

## 4 DISCUSSION

# 4.1 A possible relationship between source flux and column density

For the best-fitting two-component model described above (model 2 in Table 2), Fig. 5 shows the column of absorbing material to be inversely related to the normalization parameter of the absorbed power law, i.e. to the flux prior to absorption. As this component dominates the unabsorbed luminosity of the source, the absorbing column is inversely proportional to the source luminosity. Whilst one might initially assume any reduction in absorption with increasing flux to be due to increased ionization, we have shown that models involving varying ionization alone do not fit the data; models allowing variation of ionization and absorbing column simultaneously also

require an inverse relationship between the absorbing column and the unabsorbed luminosity and do not require the ionization to vary significantly. Fits to spectra of NGC 4151 by Lubiński et al. (2010) at different flux levels show a similar reduction in the absorbing column with increasing flux, implying that this relationship is not unique to NGC 1365. A physical mechanism is required to explain this relationship and a possible solution lies in an X-ray wind of absorbing material rising from the accretion disc.

## 4.2 AGN wind model

X-ray absorption is often attributed to outflows, in particular to a disc wind (see e.g. Kaastra et al. 2000, Blustin et al. 2005, Tombesi et al. 2013). In the AGN model proposed by Elvis (2000), absorbing material arises from a narrow range of accretion disc radii in a biconical 'wind'. Nicastro (2000) shows that an X-ray absorbing wind could originate from a narrow boundary region between the radiation pressure-dominated and gas pressure-dominated regions of the accretion disc. In these models, a rise in accretion rate, which will give rise to an increase in X-ray luminosity, naturally leads to an increase in the radii from which the wind arises through at least two mechanisms. First, a higher accretion rate leads to an increase in disc temperature and hence an increase in the radii from which the wind arises. Secondly, a higher accretion rate leads to an increased ionizing UV flux from the inner disc. When potential wind material at the disc surface is fully ionized, it is only subject to Compton scattering; the much more powerful line-driving force (Proga, Stone & Drew 1999) is no longer applicable, hence this material would never be driven off as a wind. Thus, if the inclination is such that the observer views the X-ray source through the inner edge of the wind, an increase in accretion rate would move the wind outwards such that the observer would now be viewing the source through a lower absorbing column. An additional geometric factor which would reduce absorbing column is that, in the Elvis (2000) model, an increase in X-ray luminosity causes the opening angle of the wind to increase due to the increased radiation pressure. The above affects will thus naturally lead to the inverse relationship between absorbing column and luminosity which we see. Moving the absorbing wind to larger radii also means that the line of sight would go through the less dense, more highly ionized front part of the wind, as we see in our fits.

The low ionization states found in our models suggest that the material involved is not associated with the highly ionized, high-velocity outflows suggested by Risaliti et al. (2005), which is too ionized to cause the observed X-ray absorption. We therefore suggest that the absorbing material lies in a region which is further out than this highly ionized material, as part of a stratified wind (Elvis 2000; Tombesi et al. 2013).

Depending on which mechanism dominates in pushing the wind to larger radii with increasing accretion rate, we expect different lags between the change in absorbing column and the change in luminosity which could lead to hysteresis and scatter in the X-ray luminosity/hardness relationships.

If the outward movement of the wind launch radii is caused by a change in disc temperature due to inwardly propagating accretion rate fluctuations, then the X-ray luminosity will lag by the viscous travel time of those fluctuations to either the inner edge of the disc where the seed photons are mainly produced and/or to the X-ray emitting corona itself. For typical wind launch radii of a few hundred  $R_{\rm g}$  (Higginbottom et al. 2013), this time-scale would be of the order of weeks to months.

If the outward movement of the wind is dominated by an increase in ionizing UV photons from the inner edge of the disc, which also dominate the X-ray seed photon flux, then variations in the X-ray luminosity will lead changes in the absorbing column slightly, by the difference between the light travel time from the UV region to the wind and to the corona, respectively. This difference is likely to be small (hours). Alternatively, if the wind moves outwards in response to increased UV flux, but the X-ray luminosity rises in response to increased accretion rate rather than increased seed photon flux, then the X-ray luminosity will lag by the difference between the viscous propagation time from the UV to X-ray emitting regions and the light travel time from the UV emitting to wind launch radii. This difference is also likely to be small (1–2 d).

Our observations do not show a great deal of scatter in the hardness-count rate diagram, indicating that any lags are short. We therefore favour a mechanism by which the wind launch radii are pushed outwards mainly by a rise in ionizing UV flux, rather than by a rise in local disc temperature. Regardless of mechanism by which these outflows are driven, it is clear from our data that a geometrical response to changes in luminosity is necessary in the absorber in order to explain the variability in the spectra.

Finally, we note that, in all models, the wind is expected to be clumpy, meaning short time-scale variations of the absorbing column, independent of the unabsorbed luminosity, should also occur, which would also add scatter to the relationship between X-ray luminosity and absorbing column. The spectral variations reported previously on short time-scales are probably mainly the result of fitting variations induced as clumps pass over the line of sight.

## 5 CONCLUSIONS

Swift X-ray observations of NGC 1365 over a period of six years show a large amount of spectral variability. These variations are best explained by a two-component model consisting of an unabsorbed power law and a more luminous absorbed power law; for both components, the spectral index was fixed. The normalizations of the two power laws vary together. The absorbing column of the absorbed power law varies inversely with its luminosity, an effect which is not simply due to increased ionization. This effect can be simply explained by viewing through the edge of a wind whose launch radius varies inversely with increasing accretion rate. The unabsorbed power law could be explained, as in the standard Elvis (2000) wind model, as the scattered component from the far side of the wind.

## ACKNOWLEDGEMENTS

SDC thanks the STFC for support under a studentship and IMcH thanks the STFC for support via grant ST/G003084/1. This research has made use of data obtained through the High Energy Astrophysics Science Archive Research Center Online Service, provided by the NASA/Goddard' Space Flight Center. We thank Christian Knigge and James Matthews for useful discussions.

## REFERENCES

Arnaud K. A., 1996, in Jacoby G. H., Barnes J., eds, ASP Conf. Ser. Vol. 101, Astronomical Data Analysis Software and Systems V. Astron. Soc. Pac., San Francisco, p. 17

Beloborodov A., 1999, Poutanen J., Svensson R., eds, ASP Conf. Ser. Vol. 161, High Energy Processes in Accreting Black Holes. Astron. Soc. Pac., San Francisco, p. 295 Blustin A. J., Page M. J., Fuerst S. V., Branduardi-Raymont G., Ashton C. E., 2005, A&A, 431, 111

Braito V., Ballo L., Reeves J. N., Risaliti G., Ptak A., Turner T. J., 2012, MNRAS, 428, 2516

Brenneman L. W., Risaliti G., Elvis M., Nardini E., 2013, MNRAS, 429, 2662

Cameron D. T., McHardy I., Dwelly T., Breedt E., Uttley P., Lira P., Arevalo P., 2012, MNRAS, 422, 902

Childress M. J. et al., 2013, ApJ, 770, 29

Coppi S., 1992, MNRAS, 258, 657

Dickey J. M., Lockman F. J., 1990, ARA&A, 28, 215

Done C., Mulchaey J. S., Mushotzky R. F., Arnaud K. A., 1992, ApJ, 395, 275

Done C., Madejski G. M., Smith D. A., 1996, ApJ, 463, 63

Elvis M., 2000, ApJ, 545, 63

Elvis M., Risaliti G., Nicastro F., Miller J. M., Fiore F., Puccetti S., 2004, ApJ, 615, 25

Fabian A. C., Vaughan S., 2003, MNRAS, 340, 28

Fabian A. C., Miniutti G., Iwasawa K., Ross R. R., 2005, MNRAS, 361, 795 Fabian A. C. et al., 2012, MNRAS, 419, 116

Guainazzi M., Antonelli L. A., 1999, MNRAS, 304, 15

Higginbottom N., Knigge C., Long K. S., Sim S. A., Matthews J. H., 2013, MNRAS, 436, 1390

Iyomoyo N., Makishima K., Fukazawa Y., Tashiro M., Ishisaki Y., 1997, PASJ, 49, 425

Kaastra J. S., Mewe R., Liedahl D. A., Komossa S., Brinkman A. C., 2000, A&A, 354, L83

Klotz A., Normand J., Conseil E., 2012, Cent. Bur. Electron. Telegrams, 3276, 1

Kulkers E., Wijnands R., Belloni T., Mendez M., van Der Klis M., van Paradijs J., 1998, ApJ, 494, 753

Lamer G., McHardy I. M., Uttley P., Jahoda K., 2003, MNRAS, 338, 323 Lavaux G., Hudson M. J., 2011, MNRAS, 416, 2840

Lubiński P., Zdziarski A. A., Walter R., Paltani S., Beckmann V., Soldi S., Ferrigno C., Courvoisier T. J.-L., 2010, MNRAS, 408, 1851

Maiolino R., Rieke G. H., 1995, ApJ, 454, 95

Malizia A., Stephen J. B., Bassani L., Bird A. J., Panessa F., Ubertini P., 2009, MNRAS, 399, 944

Matt G., Guainazzi M., Maiolino R., 2003, MNRAS, 342, 422

Miller L., Turner T., Reeves J., 2008, A&A, 483, 437

Nicastro F., 2000, ApJ, 530, 65

Ponti G., Miniutti G., Cappi M., Maraschi L., Fabian A. C., Iwasawa K., 2006, MNRAS, 368, 903

Pounds K., Reeves J., Page K., O'Brien P. T., 2004, ApJ, 616, 696

Proga D., Stone J. M., Drew J. E., 1999, MNRAS, 310, 476

Puccetti S., Fiore F., Risaliti G., Capalbi M., Elvis M., Nicastro F., 2007, MNRAS, 377, 607

Risaliti G., 2007, in Ho L. C., Wang J.-M., eds, ASP Conf. Ser. Vol. 373, The Central Engine of Active Galactic Nuclei. Astron. Soc. Pac., San Francisco, p. 458

Risaliti G., Maiolino R., Bassani L., 2000, A&A, 365, 33

Risaliti G., Elvis M., Nicastro F., 2002, ApJ, 571, 234

Risaliti G., Bianchi S., Matt G., Baldi A., Elvis M., Fabbiano G., Zezas A., 2005, ApJ, 630, 129

Risaliti G., Elvis M., Fabbiano Baldi A., Zezas A., Salvati M., 2007, ApJ, 659, 111

Risaliti G. et al., 2009, ApJ, 696, 160

Risaliti G. et al., 2013, Nature, 494, 449

Sobolewska M. A., Papadakis I. E., 2009, MNRAS, 399, 1597

Tombesi F., Cappi M., Reeves J., Nemmen R. S., Braito V., Gaspari M., Reynolds C. S., 2013, MNRAS, 430, 1102

Turner T., Miller L., Reeves J. N., Kraemer S. B., 2007, A&A, 475, 121

Uttley P., McHardy I. M., Papadakis I. E., Guainazzi M., Fruscione A., 1999, MNRAS, 307, 6

Wang J., Fabbiano G., Evlis M., Risaliti G., 2009, ApJ, 294, 718 Zdziarski A. A., Lubi P., Smith D. A., MNRAS, 303, 11

This paper has been typeset from a  $T_EX/I_AT_EX$  file prepared by the author.